ACS APPLIED BIO MATERIALS

www.acsabm.org

Article

Bioinspired Engineering of *Bombyx mori* Silk Fibroin: Solution Blow-Spun Nanofibers Hybridized with (3-Aminopropyl)triethoxysilane

Amanda R. Sorigotti, Rafaella T. Paschoalin, Robson Rosa da Silva, Rafaella F. Fernandes, Hernane da Silva Barud, Sidney J. L. Ribeiro, Osvaldo N. Oliveira Jr, Caio G. Otoni,* and Luiz Henrique Capparelli Mattoso*

Cite This: *ACS Appl. Bio Mater.* 2026, 9, 4170−4181

Read Online

ACCESS | Metrics & More | Article Recommendations

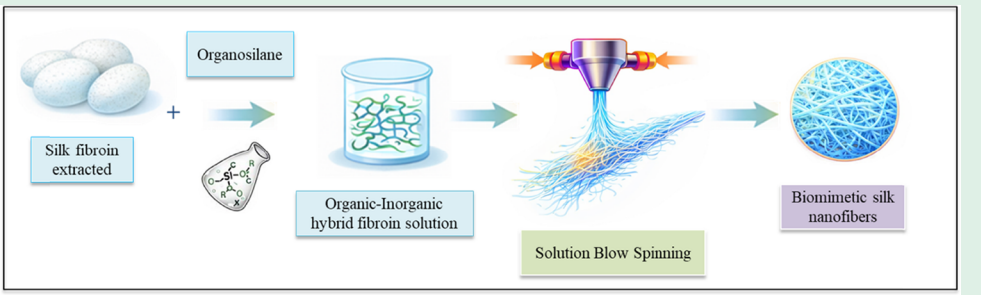

ABSTRACT: The development of bioinspired nanofibrous scaffolds with adjustable functions is essential for a range of applications, from tissue engineering to sustainable materials that exploit the hierarchical architectures of *Bombyx mori* silks. In this work, we report the production of organic−inorganic nanofibers by incorporating the organosilane (3-aminopropyl)triethoxysilane (APTES) into silk fibroin using the solution blow spinning (SB-spinning) technique. The incorporation of APTES aims to modulate solution rheological properties, promote conformational transition to β-sheet-rich structures, and increase the thermal stability of the resulting nanofiber, making them more suitable for biomedical applications. Silk fibroin was isolated from *B. mori* cocoons, dissolved in a ternary $CaCl_2$/EtOH/H_2O solution, and hybridized with APTES before fiber production. The resulting nanofibers displayed smooth, uniform morphologies and nanoscale diameters, confirming the effectiveness of SB-spinning for creating hybrid systems. Rheological analyses showed that adding APTES reduced viscosity and enhanced the processability of fibroin solutions. Spectroscopic and X-ray diffraction data revealed an increased β-sheet content and crystallinity in the hybrid fibers, while thermogravimetric analysis indicated improved thermal stability. Overall, these results demonstrate that incorporating APTES effectively alters the physicochemical and structural properties of silk fibroin, enabling the production of promising nanofibrous scaffolds for biomedical applications. This study thus introduces an approach to engineering organic−inorganic hybrid biomaterials via a scalable, low-cost spinning process.

KEYWORDS: *biopolymers, solution blow spinning, APTES, hybrid nanofibers, tissue engineering*

1. INTRODUCTION

The remarkable structural sophistication of natural silks, particularly those produced by *Bombyx mori*, has inspired strategies to replicate and engineer their hierarchical architectures. For example, through a bioinspired design approach, solution blow-spun silk fibroin nanofibers were hybridized with organosilanes to explore nature-inspired structure−property relationships and expand the functionality of regenerated silk-based biomaterials.[1−3] Scaffolds designed to mimic the structure and properties of the native extracellular matrix (ECM) have created a microenvironment that promotes cell adhesion, proliferation, and differentiation.[4−6] The ECM consists of a hierarchical network of nanofibers that guide cellular behavior through biochemical and mechanical signals.[7] Reproducing this nanoscale structure is therefore crucial for designing biomaterials with optimal biological functions. Nanofibrous scaffolds with shapes and surface areas similar to those of natural ECM have been obtained,[8,9] and can be manufactured by solution blow spinning (SB-spinning), a simple, efficient, and low-cost technique.[10,11] Unlike electrospinning, SB-spinning does not require high voltages and offers a potentially gentler processing environment for incorporating bioactive molecules or even living

Received: January 22, 2026
Revised: March 22, 2026
Accepted: April 6, 2026
Published: April 17, 2026

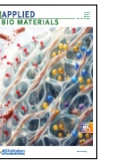

cells, although stretching stresses must be considered in specific applications.[12,13]

Choosing the right polymer is essential for scaffold performance. A primary choice may be the protein silk fibroin extracted from *Bombyx mori* due to its excellent biocompatibility, biodegradability, and mechanical strength.[14−17] This protein mainly consists of glycine, alanine, serine, and tyrosine residues arranged in amorphous (Silk I) and crystalline (Silk II) regions.[18,19] The Silk II structure, which is rich in β-sheets, provides thermal stability and resistance to enzymatic degradation, while the Silk I structure offers flexibility and solubility.[20] The ability to adjust the balance between these conformations enables silk fibroin to be customized for biomedical applications, including wound healing, drug delivery, and tissue scaffolding.[21−25] Fibroin properties can be tailored by surface functionalization or hybridization. In particular, organosilanes such as (3-aminopropyl)triethoxysilane (APTES) can react with fibroin via silanol condensation or hydrogen bonding, resulting in organic−inorganic hybrid materials with improved functionality.[26,27] These hybrids combine the flexibility and biocompatibility of proteins with the mechanical strength and chemical versatility of silanes. The presence of amine and alkoxysilane groups may enhance fibroin's hydrophobicity, thermal stability, and its ability to immobilize biomolecules such as enzymes or antibody-features that are highly desirable for tissue engineering scaffolds.[28,29]

In this work, we produced hybrid silk fibroin−APTES nanofibers via solution blow spinning. The main aim was to investigate how the addition of a representative organosilane (APTES) affects the morphology, rheology, crystallinity, and thermal properties of silk fibroin. Rather than directly replicating the natural spinning process, this study focuses on translating bioinspired principles, such as rheological control and secondary-structure modulation, into an engineered, scalable system. Moreover, organosilane hybridization promotes a shift toward β-sheet-rich (Silk II-like) conformations in regenerated silk nanofibers, thereby enhancing crystallinity and thermal stability. The results presented here demonstrate that solution blow spinning is a scalable route for producing organic−inorganic silk-based nanofibrous scaffolds with tailored structural and physicochemical properties.

2. EXPERIMENTAL SECTION

2.1. Production of Silk Fibroin/APTES Solutions

Silkworm cocoons from *Bombyx mori* were supplied by BRATAC (Bastos, Brazil). Sodium carbonate (Na_2CO_3), anhydrous calcium chloride ($CaCl_2$), ethanol P.A. (EtOH), methanol P.A. (MeOH), formic acid (98−100%), and 3-aminopropyltriethoxysilane (APTES) were purchased from Sigma-Aldrich (Brazil). All chemicals were used without any prior treatment. Fibroin was extracted from silkworm cocoons using the method described by Rockwood et al.,[30] with minor modifications. The use of a ternary $CaCl_2$/EtOH/H_2O solution for dissolution was chosen as a cost-effective and well-established alternative to LiBr, maintaining protein integrity for spinning. First, 10 g of cocoons were chopped into pieces and degummed in a solution containing 8.48 g of Na_2CO_3 and 4 L of Milli-Q deionized water at 80 °C for ca. 30 min to remove sericin. After extraction, the silk fibroin fibers were stirred at room temperature in 2L Milli-Q water for 20 min; this step was repeated three times. The fibers were dried at room temperature for 24 h. Then, 10 g of fibers were dissolved in 100 mL of a ternary $CaCl_2$/EtOH/H_2O solution at a molar ratio of 1:2:8, at 70 °C for 1 h. The resulting viscous solution was dialyzed against ultrapure water for 48 h, six times. The solution was then centrifuged at 9000 rpm (Rotina 380, Andreas Hettich GmbH & Co., Germany) at 4 °C for 20 min to remove undissolved impurities; this step was repeated twice. Finally, the solutions were frozen at −25 °C for 12 h and subsequently lyophilized (Supermodulyo Freeze Dryer, Thermo Electron Corporation, USA) for 72 h. Solutions of pure fibroin at concentrations of 10% and 12% (w/v, considering the mass of hydrated fibroin) were prepared by dissolving the protein in 16 mL of formic acid at room temperature and stirring for 3 h. To create hybrid nanofibers using organosilanes, after the protein was fully dissolved, 10% (w/v, relative to the mass of dry fibroin) APTES was added to the solution and stirred for an additional 30 min. The linear viscoelastic region was determined for each sample via preliminary amplitude sweeps, and subsequent frequency sweeps were performed within this region using a constant stress of 0.1 Pa. The rheological behavior of the solutions was studied using a rotational rheometer with double gap geometry (MCR 301, Anton Paar GmbH, Austria). Measurements were carried out at room temperature in both steady and oscillatory states. Steady-state measurements involved two consecutive shear cycles, where the shear rate was increased from 0 to 10 s^{-1} and then from 10 to 100 s^{-1}. At the end of these tests, viscosity and flow curves were obtained. The oscillatory measurements were performed within the linear viscoelastic region, with angular frequencies ranging from 10 to 500 rad·s^{-1}. Data on the storage and loss moduli were analyzed as functions of angular frequency.

2.2. Spinning Silk Fibroin/APTES Nanofibers

The SB-spinning apparatus used to produce silk fibroin nanofibers consisted of a system with two concentric nozzles. The polymer solutions were fed through the inner nozzle at a rate of 7 mL·h^{-1}. This rate was controlled by an injection pump (NE-1010-US One Channel 100 lb, New Era, United States) with a 20 mL glass syringe (Artglass, Italy) containing the polymer solution. In the outer nozzle, a flow of pressurized air, heated to ca. 35 °C, was maintained at a constant pressure of 2 bar. Mild heating reduced relative humidity and promoted solvent evaporation, thereby increasing spinning efficiency. Additionally, two glass rods (10 cm in length) spaced 7 cm apart were placed between the nozzles and the collector. As reported by Jia et al.,[31] the inclusion of these rods enabled the formation of well-adhered, aligned fiber bundles. The resulting nanofibers were directly deposited onto a static cylindrical metal rod collector, positioned at a working distance of 30 cm from the nozzles (Figure 1).

The silk fibroin nanofibers were immersed in pure methanol for 30 min to induce the transition from α-helix/random coils to the secondary structure of the protein, β-sheet. After immersion, the nanofibers were rinsed in deionized water for 10 min to remove excess methanol, then dried in an oven for 24 h.

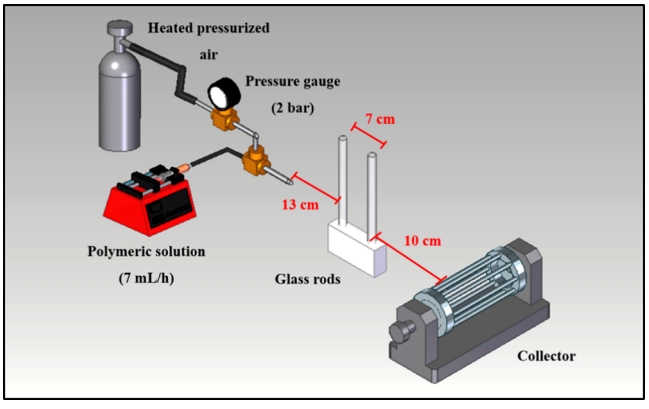

Figure 1. Schematic representation of the SB-spinning apparatus with heated pressurized air and glass rods used to produce nanofibers.

https://doi.org/10.1021/acsabm.6c00155
ACS Appl. Bio Mater. 2026, 9, 4170−4181

2.3. Nanofiber Characterization

Nanofibers were characterized by scanning electron microscopy (SEM) and atomic force microscopy (AFM) for morphological analysis. For SEM, a DSM960 microscope (Carl Zeiss, Germany) was used at an acceleration voltage of 10 kV and a working distance of 10 mm to image the nanofiber mats, which had been previously coated with a thin gold layer using a sputter coater (SCD 050, Bal-Tec, USA). Images acquired at the highest magnification (5000×) were used to measure nanofiber cross-sectional diameters in ImageJ (version 1.52a). At least 100 fibers were analyzed to determine the mean diameter, standard deviation, and diameter distribution. Nanofibers prepared for AFM measurements from silk fibroin solutions at 10% and 12% (w/v) containing 10% (w/w) APTES were deposited during spinning onto silicon substrates coated with a 10-nm layer of white gold. The images were obtained using the FlexAFM Sample Stage microscope (Nanosurf, Switzerland) and processed using Gwyddion software, version 2.52.

The hydrophilic or hydrophobic properties of pure fibroin nanofibers containing APTES were assessed by measuring the contact angle of deionized water on their surface using an automatic optical goniometer (CAM 101, KSV Instruments, Finland). For each measurement, 2−3 μL of deionized water was placed on the nanofiber surface, and images were automatically captured every 1 s for 1 min. The average contact angle at each time point was calculated as the mean of the angles measured at the left and right ends using the KGV-500 software. The average contact angle and its standard deviation were determined from images taken at 5 s for three different measurements. The thermal behavior of pure and hybrid silk fibroin nanofibers was analyzed by thermogravimetry (TA Q500, TA Instruments, USA) under both inert and oxidative conditions. In the inert atmosphere, samples were heated from 25 to 900 °C at 10 °C min^{-1} with nitrogen flowing at 60 mL·min^{-1}, whereas in the oxygen-containing atmosphere, the samples were heated from 25 to 700 °C at the same heating rate.

Infrared spectra were obtained using a Fourier-transform infrared (FTIR) spectrometer (Vertex 70, Bruker, Germany) with an attenuated total reflectance (ATR) accessory. A total of 128 scans were recorded over the wavenumber range of 4000−600 cm^{-1}, with a spectral resolution of 2 cm^{-1}. To complement the FTIR results, Raman spectroscopy of the samples was performed using a Vertex 70 (Bruker, Germany) equipped with a germanium detector (Ge). The analysis was conducted using 200 scans at a resolution of 4 cm^{-1} and a laser power of 500 mW. The OPUS 6.0 software (Bruker Optik, Ettlingen, Germany) was used to acquire the data for this analysis.

AFM was combined with infrared spectroscopy (AFM-IR) to examine the surface functional groups of silk fibroin nanofibers and the protein's conformation at various points along the fibers. Samples were prepared following the same procedure as standard AFM techniques. Analyses were conducted using the NanoIR 2S device (Anasys Instruments, Germany), and spectra with wavenumbers between 1800 and 1570 cm^{-1} were collected from multiple areas of the nanofibers. Data analysis was carried out using Analysis Studio. The arithmetic (Ra) and quadratic (Rq) mean surface roughness values were obtained directly from the analysis of the AFM topography images using the statistical tools provided by the Gwyddion software.

X-ray diffraction (XRD) was used to determine the crystal structure of silk fibroin nanofibers produced by SB-spinning. Nanofiber mats were analyzed using a LabX XRD-6000 diffractometer (Shimadzu Co., Japan) with Cu K_α radiation (λ = 0.15428 nm), 30 kV, and 30 mA. Scans were recorded continuously over Bragg angles (2θ) from 5° to 70° at a scan rate of 1° min^{-1}. The interplanar distance (d) for each scattering angle (2θ) was determined by the Bragg equation (eq 1).

$$d = \frac{\lambda}{2\,sin(\theta)} \tag{1}$$

To estimate the degree of crystallinity, the XRD patterns obtained were initially subjected to peak deconvolution analysis. The diffraction data were fitted with Gaussian functions using OriginPro 8.0. Goodness-of-fit was assessed using the coefficient of determination (R^2), which indicates how well the statistical model represents the experimental data. The index of crystallinity (CI, %) was calculated as the ratio of the cumulative area of the crystalline peaks to the total area under the diffraction curve, as described by eq 2.[32] Crystalline peaks were identified based on the characteristic reflections of the silk fibroin β-sheet conformation. All peak integration procedures were performed using the built-in analytical tools of OriginPro 8.0 to ensure high precision in the area calculations:

$$\mathrm{CI}\ (\%) = \frac{\sum \mathrm{area}_{\mathrm{crystalline}}}{\sum \mathrm{area}_{\mathrm{total}}} \times 100 \tag{2}$$

Where:

$\sum \mathrm{area}_{\mathrm{crystalline}}$: sum of areas of Silk I and Silk II peaks.

$\sum \mathrm{area}_{\mathrm{total}}$: total area including the amorphous peak.

The quantitative data from the analyses are presented as means and standard deviations from repetitions. The statistical methods of analysis of variance (ANOVA) and the Tukey test were used to determine the effect of solution concentration on mean nanofiber diameter. One-way ANOVA showed no significant difference in nanofiber diameters at the 0.05 significance level. All charts were created using OriginPro 8.0.

3. RESULTS AND DISCUSSION

The SEM images in Figure 2 indicate a smooth, homogeneous microstructure of the high-aspect-ratio SB-spun fibers, regardless of composition. The AFM analysis (see insets in Figure 2) confirms that this surface uniformity extends to the nanoscale, with no defects or phase separation. From the AFM-IR data (Figure 3), we inferred that APTES was evenly grafted onto the SB-spun fibers. The diameter remained constant along the fiber length, a typical feature of SB-spun constructs that is not affected by surface modification with APTES.[1−3,11] The few inhomogeneities (e.g., beads) along the nanofibers may originate from jet instability or incomplete solvent evaporation during the spinning process.[11,31,33] Among the various concentrations tested, the APTES-free 10% and APTES-added 12% solutions exhibited the best spinnability, with their jets remaining stable, leading to more uniform, defect-free fibers. This was not true for less concentrated—i.e., 8% (w/v)—or more concentrated—i.e., 14% (w/v)—solutions, which either produced fibers with many defects (in the first case) due to turbulent flow from the too thin system, or no fibers at all (in the second case) because of spinneret clogging caused by the overly thick fluid. AFM provided additional information on the fibers' topography. Both the arithmetic (Ra) and quadratic (Rq) mean surface roughness increased—from 3 ± 1 to 6 ± 2 nm (Ra) and from 4 ± 1 to 8 ± 2 nm (Rq)—after APTES was incorporated into the silk fibroin fibers. A similar result was reported for different surfaces[34−36] and has been linked to APTES aggregation along the fiber surface during silanization.[37]

The size distribution histograms in Figure 2 reveal that all fiber diameters are in the nanoscale. Still, the population shifts toward either thicker or thinner nanofibers based on the composition of the precursor solution. APTES-free nanofibers exhibited notably similar diameters (491 ± 138 nm for 10% (w/v) and 509 ± 147 nm for 12% (w/v)). For each condition, at least 100 fibers were analyzed to determine the mean diameter and standard deviation. APTES-containing counterparts are

https://doi.org/10.1021/acsabm.6c00155
ACS Appl. Bio Mater. 2026, 9, 4170−4181

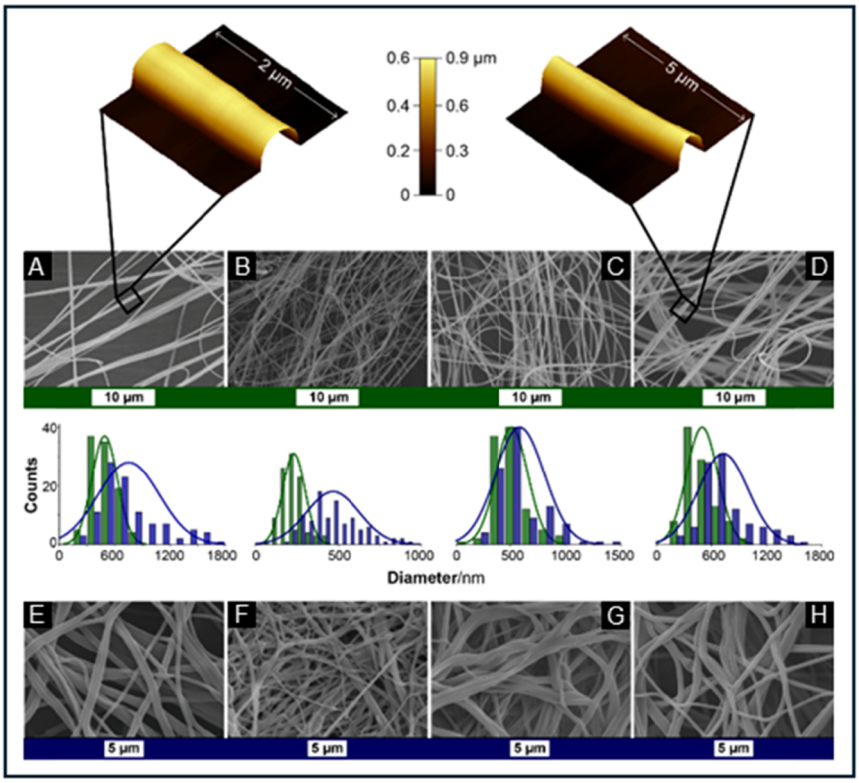

Figure 2. Morphological characterization of solution blow-spun nanofibers and the comparative average fiber diameter distribution before and after methanol treatment. (A–D) Representative SEM images of silk fibroin (SF) nanofibers: (A) SF10, (B) SF10 + APTES, (C) SF12, and (D) SF12 + APTES. (E–H) Corresponding SEM images after methanol treatment (MeOH): (E) SF10-MeOH, (F) SF10 + APTES-MeOH, (G) SF12-MeOH, and (H) SF12 + APTES-MeOH. Sample codes: SF10 and SF12 refer to 10 and 12% (w/v) silk fibroin concentrations, respectively; "+APTES" indicates the incorporation of 10% (w/w) organosilane. Scale bars represent different length scales for all images.

thinner – this diameter reduction is more significant (approximately 54%) for nanofibers from 10% (w/v) fibroin solutions containing the organosilane (227 ± 67 nm). Interestingly, post-spinning methanol treatment causes a notable change in nanofiber morphology through swelling, resulting in increased crimp along the fiber length and tighter adhesion between neighboring nanofibers. Swelling is evidenced by the larger diameters of methanol-treated nanofibers (blue histograms in Figure 2) compared to their untreated counterparts (green histograms). Although swollen, the fibers remain submicrometric in diameter. For example, fibroin-only fibers from 10% and 12% (w/v) solutions exhibit 54% and 15% larger diameters (756 ± 334 and 587 ± 222 nm, respectively) than their untreated analogues. In the case of fibroin/APTES hybrids, more substantial variations (106% and 47% increases in diameter from fibers made with 10 and 12% (w/v) fibroin solutions, respectively) are caused by methanol, resulting in average diameters of 469 ± 160 nm and 732 ± 269 nm.

Although silk fibroin constructs are commonly treated with methanol,[38−40] the morphological effects of this practice are seldom documented. Dehghan-Manshadi et al.,[41] who observed a morphology similar to ours after immersing electrospun silk fibroin nanofibers in methanol, attributed the swollen, crimped structure to the relaxation of previously quenched, elongated fibroin chains. According to Pavlova et al.,[42] the morphological change can be explained by the swelling of fibroin within the first few seconds of immersion in methanol, followed by a rapid decrease in the surface area of the mats, which accounts for ca. 40% of our nanofibers. This shrinkage is accompanied by two main morphological changes: crimping of the nanofibers and an increase in their diameters, both attributed to the release of residual stress resulting from the high elongational flow experienced by the polymer chains during spinning.[43−45] When sufficient degrees of freedom are provided, in this case by adding methanol, the chains spontaneously adopt their lower-energy—and therefore most stable—conformation through an entropically driven relaxation process.[42,46]

The average nanofiber diameter depends mainly on two factors: solution concentration and the addition of APTES. According to the steady-state viscosity measurements shown in Figure 3A, viscosity increases as the solution concentration rises from 10% to 12% (w/v). At a shear rate of 10 s^{-1}, where a transition occurs from shear thinning behavior (viscosity decreases with increasing shear rate) to Newtonian behavior (constant viscosity regardless of shear rate), a 61% increase in viscosity is observed for solutions containing only silk fibroin, and a 38% increase for their hybrids with APTES. This pattern is consistent with findings by Magaz et al.[1] and Zhu et al.[19] for silk fibroin in formic acid solutions at concentrations below 20% (w/v). Higher polymer concentrations lead to greater chain entanglement, making it more difficult to align them in the flow direction and thereby increasing viscosity.[18] Regarding the APTES effect, at the same concentration, viscosity decreases with the addition of the organosilane. Unlike solutions containing only silk fibroin, upon addition of APTES, the rheological behavior becomes Newtonian at low shear rates (< 10 s^{-1}).

https://doi.org/10.1021/acsabm.6c00155
ACS Appl. Bio Mater. 2026, 9, 4170−4181

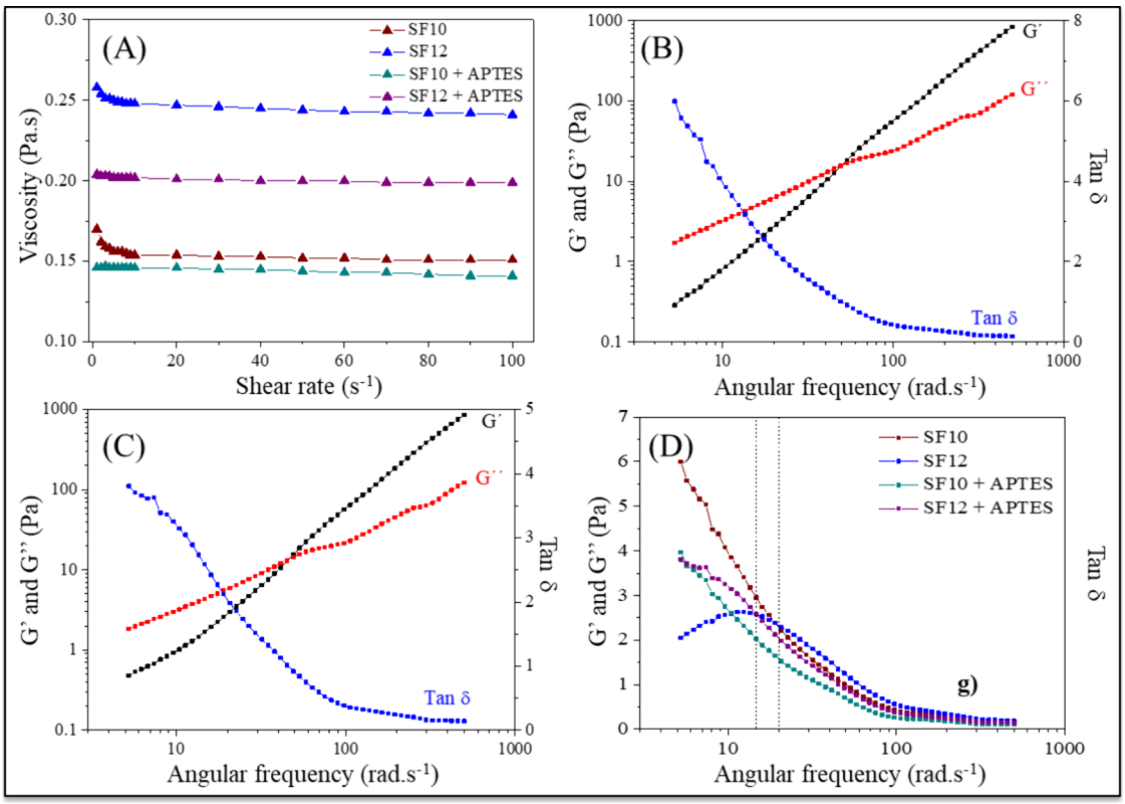

Figure 3. Rheological characterization of silk fibroin and hybrid SF/APTES solutions. (A) Steady-state flow curves showing shear viscosity as a function of the shear rate for all conditions. (B, C) Dynamic frequency sweeps presenting the storage modulus (G', filled symbols) and loss modulus (G", open symbols) for representative samples: (B) SF10 and (C) SF12 + APTES, illustrating the viscoelastic behavior of pure and hybrid systems at different concentrations. (D) Comparative analysis of the viscoelastic crossover point (G' = G") for all samples, indicating the transition from viscous-dominant to elastic-dominant behavior. Sample codes: SF10 and SF12 refer to 10 and 12% (w/v) silk fibroin concentrations; "+APTES" indicates 10% (w/w) organosilane. Measurements performed at 25 °C within the LVER.

Although APTES has a low molecular weight (221.37 g·mol^{-1}) compared to silk fibroin, the interaction between the organosilane and the protein chemical groups increases the distance among its polymeric chains. Hence, secondary interactions, as well as chain entanglements and interchain interactions, decrease, while the free volume increases. These factors provide less resistance to flow during rheological analysis, resulting in lower solution viscosity.

The observed reduction in average nanofiber diameter is explicitly linked to the rheological changes. The decrease in viscosity and the shift in the viscoelastic crossover frequency indicate that the addition of APTES makes the solution more fluid and less resistant to elongational flow, facilitating more efficient jet stretching during the SB-spinning process.

Regarding rheological behavior, the nearly Newtonian flow curves observed particularly for the APTES-containing solutions are reminiscent of Boger fluid behavior, in which a constant shear viscosity coexists with significant elasticity. This rheological profile, accurately captured by shear rheometry, provides the necessary insights into the viscoelastic relaxation and stretching response required to understand the spinning stability of these hybrid dopes.

The linear viscoelastic properties of the solutions—namely, the storage (G′) and loss (G″) shear moduli, along with the loss factor (Tan δ)—were assessed using oscillatory rheology (Figure 3B–D). All solutions exhibit two distinct regions: one where the elastic modulus exceeds the viscous modulus (G′ > G″) at higher frequencies, and another where the viscous modulus is greater than the elastic (G′ < G″) at lower frequencies.[15−17] This suggests that the applied oscillations were faster than the polymer chain relaxation time at high frequencies. Conversely, at low frequencies, the opposite is observed: the oscillations are slower than the molecular relaxation.[14,17,47,48] Therefore, there is an increase in G′ and G″ modulus as the concentration of the solutions increases. However, the gap between them decreases until the crossover frequency (G′ = G″) is reached. The crossover frequency rose from 50 to 59 rad·s^{-1} as the concentration increased from 10% to 12% (w/v) in solutions without APTES. This occurs because more concentrated solutions exhibit longer relaxation times as silk fibroin chains become partially entangled, shifting the crossover frequency to higher values.[18] After adding APTES, both the crossover frequency and the moduli decrease, indicating that the transition from viscous to elastic behavior happens earlier than in solutions without APTES. Hence, this change in the crossover frequency suggests that APTES interacted with the silk fibroin chains.

Note that all solutions exhibited viscoelastic behavior within 0° < δ < 90°. For angular frequencies above 20 rad·s^{-1}, the solutions with concentrations of 10% and 12% (w/v) containing APTES have intermediate Tan δ values compared to other solutions, indicating that their plasticity is higher than that of

https://doi.org/10.1021/acsabm.6c00155
ACS Appl. Bio Mater. 2026, 9, 4170−4181

the 10% (w/v) solution with APTES, and their elasticity is lower than that of the 12% (w/v) solution. During spinning, it is ideal for plasticity to exceed elasticity, enabling the formation and stabilization of the jet. However, elasticity must also be present for jet initiation.[49] Therefore, the balance between plasticity and elasticity is more suitable for solutions of 10% (w/v) and 12% (w/v) with APTES. This balance contributed to a more stable spinning process, producing nanofibers with fewer defects.

It is noteworthy that the observed reduction in viscosity and the shift in viscoelastic crossover behavior upon APTES addition are consistent with bioinspired principles observed in natural silk spinning dopes, in which controlled molecular interactions enable flow under shear while preserving chain alignment. In this sense, organosilane hybridization can be regarded as an engineering strategy inspired by the rheological optimization found in *Bombyx mori* silk spinning, rather than a direct replication of the natural system.

A more detailed analysis of the chemical groups in the nanofibers and the effect of methanol was conducted using atomic force microscopy combined with infrared spectroscopy (AFM-IR) (Figure 4). This technique was especially useful for assessing conformational changes in silk fibroin across different regions of the nanofibers and for examining the distribution of APTES at the nanoscale.[50−52] In the spectra of nanofibers obtained in both concentrations, the most intense band corresponds to the amide I of the silk fibroin, which relates to the stretching vibrations of the C═O bonds, with minor contributions from N-H bending and C-N stretching.[53] For 10% (w/v) nanofibers, this band appears at 1656 cm^{-1} in the blue curve and at 1654 cm^{-1} in the regions highlighted in red and purple in Figure 4A, respectively. Although there is a slight variation in band position, all of them indicate that the conformation of silk fibroin is a combination of random coil and α-helix.[28,54] The amide I band slightly narrowed and shifted to higher wavenumbers upon addition of APTES, ranging from 1659 (orange spectrum) to 1667 cm^{-1} (purple spectrum), depending on the analyzed region. This shift is related to the scissoring bending vibration of the NH_2 groups of APTES, indicating that this organosilane has interacted with the protein structure.[55] Additionally, this suggests an increase in structures with β-sheet conformation, resulting from the transition from Silk I to Silk II after functionalization with APTES,[56] a finding also reported by da Silva et al.[57] for silk fibroin films with varying amounts of (3-glycidyloxypropyl) trimethoxysilane (GPTMS).

Thus, the chemical modification of silk fibroin with APTES molecules follows the mechanism described by Sagnella et al.[58] The reactive hydroxyl (-OH) groups present in serine and tyrosine residues, which together constitute approximately 12−17% of the protein, serve as the primary sites for functionalization. At serine residues, these groups are extensively exposed at the N-terminus of the fibroin structure, making them highly accessible for chemical modification (Figure 5). The functionalization process forms covalent Si-O bonds between the organosilane and the protein matrix. This allows APTES to act as a bifunctional linker, connecting the silk fibroin backbone

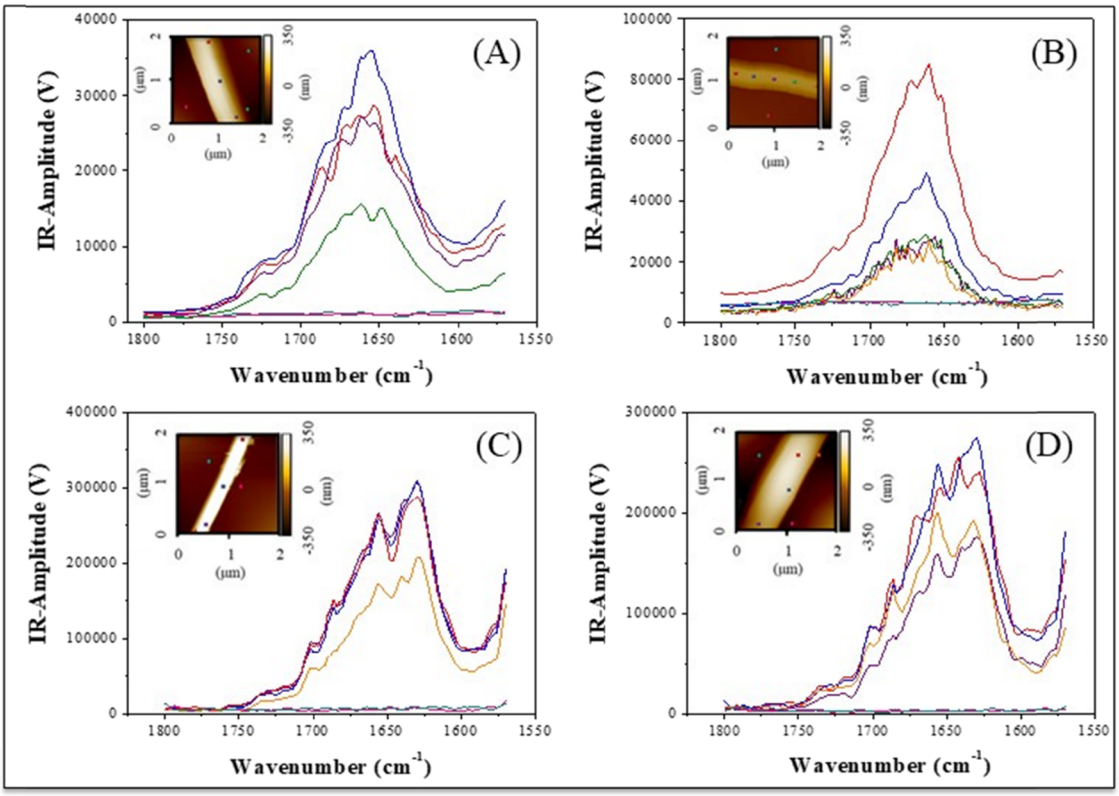

Figure 4. AFM topography images and corresponding IR absorption maps at 1650 cm^{-1} (Amide I) for representative hybrid nanofibers: (A, B) SF10 + APTES and (C, D) SF12 + APTES. The color scale in topography represents height variations, in which the IR spectra collected at specific points along the nanofibers show the characteristic absorption bands of silk fibroin and APTES. All images were processed using Gwyddion software to ensure topographical accuracy.

https://doi.org/10.1021/acsabm.6c00155
ACS Appl. Bio Mater. 2026, 9, 4170−4181

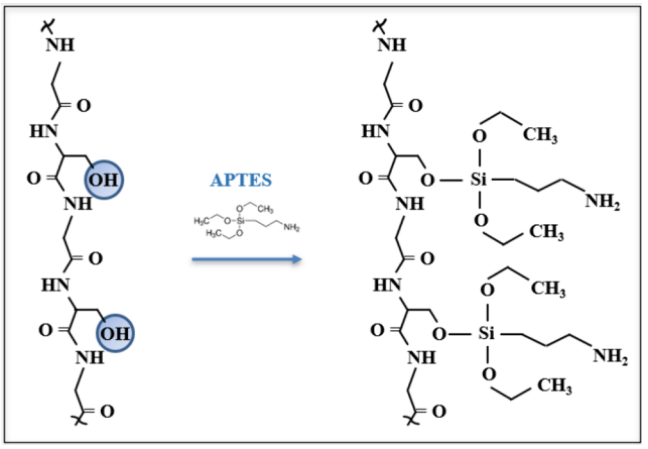

Figure 5. Schematic representation of the silk fibroin backbone highlighting the reactive hydroxyl (-OH) groups of serine and tyrosine residues, particularly those exposed at the N-terminal regions, where the chemical interaction between the APTES and the protein matrix occurs, illustrating the likely formation of covalent Si−O bonds through the condensation of silanol groups with the amino acid side chains.

through its terminal amine groups to other (bio)molecules of interest, such as antibodies or enzymes, thereby expanding the functional potential of the hybrid nanofibers.

Among the bands related to the vibrations of the amide groups in silk fibroin, the amide I band is one of the most used to describe the secondary structure of the protein.[59] Thus, the APTES-free nanofibers' crystallinity increases after immersion in methanol. This increase is evidenced by the narrowing of the band associated with the amide I of silk fibroin and its shift to lower wavenumbers,[60] specifically to 1629 cm^{-1} across all regions evaluated. Methanol is well known for promoting the conversion of the silk fibroin conformation from Silk I, which is mainly α-helix and random coil, to Silk II, where the content of secondary structures with β-sheet conformation is higher than the others.[61] Methanol is a hydrophilic agent with strong dehydrating property[57] and, therefore, it attracts the water molecules in silk fibroin due to its polarity. This interaction induces the aggregation of hydrophobic amino acids that make up the protein, primarily alanine and glycine, which are the main components of the crystalline regions of the protein[62]. Thus, methanol promotes crystallization by increasing the prevalence of β-sheet structures while excluding hydrophobic amino acids. Regarding the morphological changes after methanol treatment, the observed increase in diameter (swelling) is attributed to the relaxation of residual stresses induced during spinning. While methanol acts as a molecular dehydrating agent, promoting β-sheet formation, it simultaneously allows the polymer chains to adopt a lower-energy conformation macroscopically.

The secondary conformations of silk fibroin were analyzed with the XRD data in Figure 6. For nanofibers not treated with methanol, a peak appears at 2θ = 9.6°, and a more intense one at 2θ = 20.6°, corresponding to interplanar distances (d) of 9.2 Å and 4.3 Å, respectively. These results suggest that the nanofibers have an amorphous structure characteristic of the Silk I conformation. After adding APTES, the weak peak shifts to 2θ = 10.6° (d = 8.3 Å), while a broad halo appears at 2θ = 21.1° (d = 4.2 Å), which is sharper than that observed for the non-functionalized silk fibroin nanofibers. Although the first peak clearly relates to the Silk I conformation, the emergence of the other peak at a d-spacing of 4.2 Å indicates a combination of Silk I and Silk II conformations.[45] This increase in β-sheet content following APTES addition aligns with the AFM-IR results. After immersion in methanol, the positions of these diffraction peaks shift. The low-intensity peak at 2θ = 9.6° disappears for silk fibroin nanofibers without APTES, and a broad halo appears at 2θ = 19.5° (d = 4.5 Å). Additionally, there are moderate peaks at 2θ = 25.7 and 29.6° (d = 3.5 Å and 3.0 Å, respectively). These results are characteristic of silk fibroin materials post-treated with methanol,[63] where the first peak indicates the transition to the Silk II conformation, and the more intense peaks suggest a mix of Silk I and Silk II conformations.[64] For the hybrid nanofibers, a small peak at 2θ = 9.1° (d = 9.7 Å) and a stronger peak at 2θ = 19.5° (d = 4.5 Å) are observed, which are typical of the Silk II conformation.[65] The shoulder at 2θ = 29.6° (d = 3.0 Å) can be attributed to a combination of both conformations. Therefore, the materials show an increased content of Silk II conformations after immersion in methanol, consistent with the AFM-IR results, thereby enhancing the nanofibers' crystallinity.

To quantitatively assess the impact of APTES hybridization on the secondary structure of silk fibroin nanofibers, a detailed deconvolution of the XRD patterns was performed using Gaussian functions, following the methodology established by Matter, 2024, 7, 620−639. This approach enabled calculation of the Crystallinity Index (CI) for each sample, providing a robust quantification of β-sheet content. The results are presented in Table 1.

These quantitative findings provide a robust estimate of the β-sheet content, aligning with the methodology described by Cheng et al.[32] For nanofibers not treated with methanol, SF10 exhibits a CI of 25%, while SF12 + APTES shows a CI of 31%. This suggests that the addition of APTES to the SF12 solution, even without methanol treatment, increases β-sheet content, indicating a mixture of Silk I and Silk II conformations, consistent with AFM-IR results.

After immersion in methanol, the CI for the SF10-Methanol sample increases significantly to 36%, confirming the transition to the Silk II conformation and an overall increase in crystallinity. For the hybrid nanofibers SF12 + APTES-Metanol, the CI is 26%, lower than that of SF12 + APTES without methanol. This reduction in CI for the hybrid nanofibers after methanol treatment suggests a complex interplay where APTES might interfere with the complete transition to highly ordered Silk II structures, or that the initial increase in β-sheet content due to APTES is partially offset by other factors during methanol treatment.

The thermal stability of silk fibroin nanofibers and their APTES hybrids was analyzed by thermogravimetry (TG) under an oxidative atmosphere. Figure 7 shows the different mass-loss rates during the three main stages below 400 °C. The first stage, between 30 and 110 °C, with a peak at 56 °C in the TG derivative curve (DTG), corresponds to water loss and to other solvents adsorbed in the silk fibroin network, such as formic acid used in the solution preparation. The second stage, from 140 to 245 °C, is specific to nanofibers and is absent in lyophilized silk fibroin. This stage features peaks at 187 °C for the hybrids and 215 °C for silk fibroin nanofibers. The third stage, occurring between 245 and 375 °C with a maximum near 282 °C, involves thermal degradation of silk fibroin. This process entails breaking peptide bonds and decomposing residual amino acid side chains, producing low-molecular-weight gases such as

https://doi.org/10.1021/acsabm.6c00155
ACS Appl. Bio Mater. 2026, 9, 4170−4181

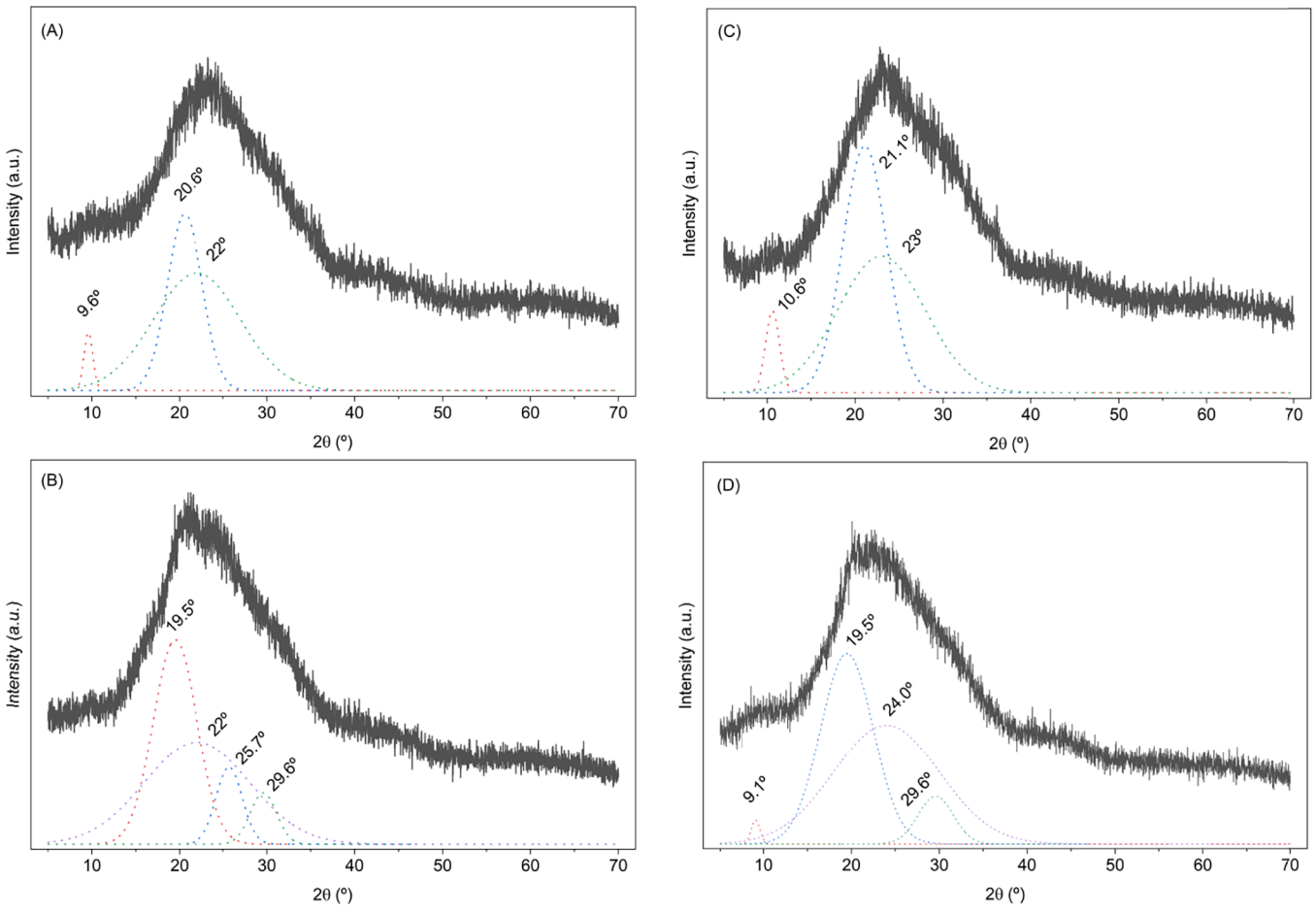

Figure 6. XRD deconvolution analysis of silk fibroin (SF) nanofibers. (A) Pure SF nanofibers (SF10); (B) pure SF nanofibers after methanol treatment (SF10-MeOH), indicating the transition to Silk II conformation with a prominent peak at 19.5° and additional peaks; (C) hybrid SF/APTES nanofibers (SF12 + APTES) before methanol treatment, showing a shift in Silk I peaks and a sharper halo. (D) Hybrid SF/APTES nanofibers after methanol treatment (SF12 + APTES-MeOH), displaying typical Silk II peaks at 9.1°, 19.5°, and a shoulder at 29.6°. The solid black lines represent experimental data, while the dotted lines indicate the individual deconvoluted crystalline peaks and the amorphous halo.

Table 1. Crystallinity Index (CI) Values for Silk Fibroin Nanofibers with and without APTES and with/without Methanol Treatment, Calculated from XRD Peak Deconvolution

sample	treatment	peak (2θ)	structure	CI (%)
SF10	without methanol	9.6° 20.6° 22.0°	Silk I Silk I amorphous	25
SF10	with methanol	19.5° 25.7° 29.6° 22.0°	Silk II Silk II Silk II amorphous	36
SF12 + APTES	without methanol	10.6° 21.1° 23.0°	Silk I Silk I/Silk II amorphous	31
SF12 + APTES	with methanol	9.1° 19.5° 29.6° 24.0°	Silk II Silk II Silk II (shoulder) amorphous	26

CO, CO_2, and NH_3. The final mass loss, observed between 425 and 600 °C, likely results from the breakdown of the main chain and the oxidation of organic material in an oxygen-rich environment. APTES affects the thermal behavior of nanofibers. At 300 °C, the mass loss of the hybrid is 29.6%, which is lower than that of lyophilized silk fibroin at 31.2%, but nearly equal to that of silk fibroin nanofibers. The mass loss of APTES-treated nanofibers becomes more pronounced at temperatures above 550 °C than at lower temperatures. Additionally, the onset of mass loss stages shifts to higher temperatures after adding the organosilane. This suggests that its addition increased the thermal stability of the protein, a fact confirmed by the residual mass at the end of the process: 0.6% and 0.7% for lyophilized silk fibroin and silk fibroin nanofibers, respectively, while 1.9% is observed for the hybrids with APTES. Similar findings were reported by Jiang et al.[66] after modifying the surface of cellulose/poly(lactic acid) composites with APTES, in which organosilane functionalization enhanced the materials' thermal stability to some extent.

Regarding the thermal stability analyzed by thermogravimetry (Figure 7), it is important to note that although the general degradation profiles of pure silk fibroin and its hybrid counterparts appear similar, subtle differences in residual mass and shifts in degradation peaks are clearly indicative of successful APTES incorporation and its stabilizing effect. Specifically, the higher residual mass in the hybrids (1.9%) compared to pure fibroin (0.6−0.7%) corresponds to the inorganic silica residue,

https://doi.org/10.1021/acsabm.6c00155
ACS Appl. Bio Mater. 2026, 9, 4170−4181

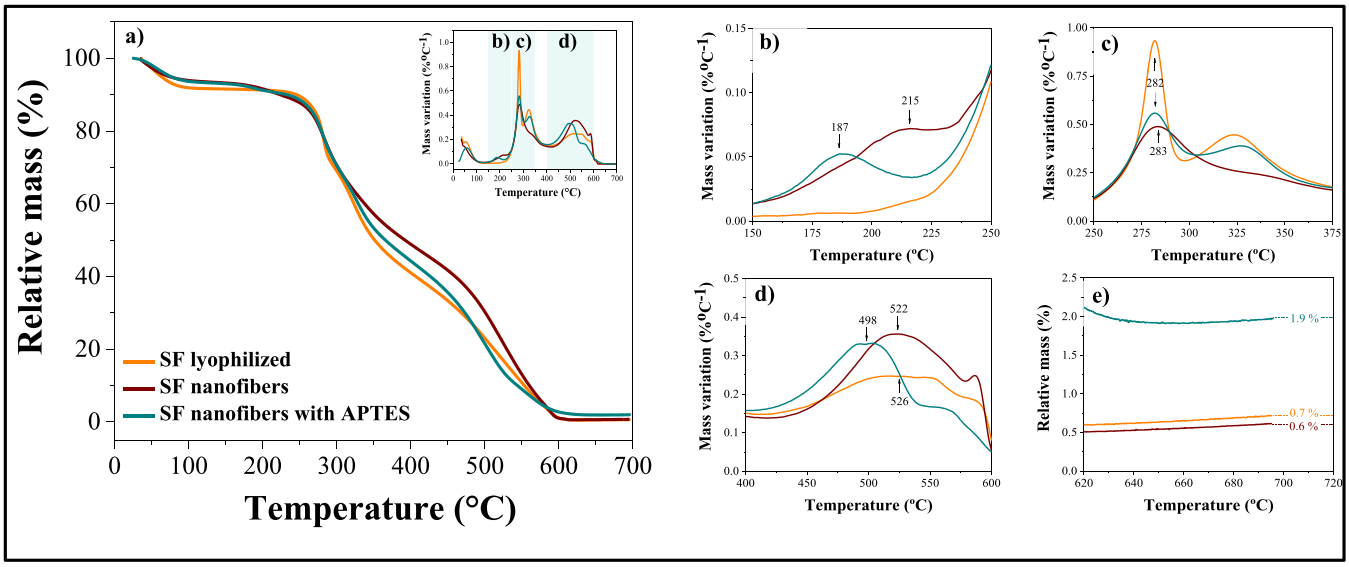

Figure 7. TG and DTG curves of freeze-dried fibroin, silk fibroin nanofibers, and their hybrids with APTES in an oxidative environment: (a) complete TG curves (25−700 °C); (b) second stage region (140−245 °C); (c) third stage region (245−375 °C); (d) final stage region (425−600 °C); and (e) residual mass values for all three samples.

while the shift of mass loss stages to higher temperatures confirms the strong intermolecular interactions between the organosilane and the protein matrix.

4. CONCLUSIONS

The successful fabrication of silk fibroin nanofibers hybridized with APTES via solution blow spinning demonstrates the feasibility of producing organic−inorganic hybrid scaffolds using a scalable, cost-effective method. The combination of fibroin's natural biocompatibility and the functional versatility of organosilanes led to nanofibrous materials with customized structural and physicochemical properties, making them highly suitable for tissue engineering applications. The incorporation of APTES significantly altered the rheological behavior of fibroin solutions, reducing viscosity and promoting the formation of stable jets during spinning. These effects are due to intermolecular interactions between amino and silanol groups, which enhance the free volume and flexibility of the polymer chains. Morphological analysis confirmed that adding APTES yielded uniform, defect-free nanofibers with smaller diameters, indicating that the hybridization process does not hinder fiber formation but rather improves processability. Spectroscopic and structural analyses revealed that adding organosilane shifts the conformation from Silk I to Silk II, increasing β-sheet content and crystallinity. This change improves thermal stability and mechanical strength, meeting the needs for long-term scaffold performance in body environments. The enhanced stability observed in thermogravimetry supports strong intermolecular interactions between the inorganic silane regions and the protein matrix.

The results, therefore, highlight the synergistic effect of organic−inorganic hybridization: APTES improves the processability, structural order, and resistance to degradation of fibroin. The ability to adjust these parameters via a straightforward solution-based approach opens new possibilities for designing nanostructured scaffolds with customizable surface chemistry and mechanical properties. Additionally, the use of the SB-spinning technique, which avoids high voltages and supports large-scale production, positions this approach as a practical alternative to traditional electrospinning for the manufacture of biomedical materials.

The pioneering creation of organic-inorganic hybrid materials by incorporating APTES into fibroin nanofibers using solution blow spinning establishes a new paradigm for developing functional silk fibroin−organosilane hybrid nanofibers, combining the biological advantages of natural polymers with the tunability of inorganic chemistry. Rather than directly replicating natural silk fibers, we showed in this study that bioinspired principles derived from *Bombyx mori* silk, particularly the control of solution rheology and secondary structure, can be translated into an engineered, scalable system for producing functional hybrid nanofibers. Future work should examine their biological performance, including cell adhesion, proliferation, and differentiation, to fully assess their potential for tissue regeneration and as implantable biomaterials. This could open new avenues in tissue engineering by enhancing the functionality of nanofibers.

■ AUTHOR INFORMATION

Corresponding Authors

Caio G. Otoni – *Institute of Chemistry, University of Campinas (Unicamp), Campinas, São Paulo 13083-970, Brazil; Graduate Program in Materials Science and Engineering (PPGCEM), Federal University of São Carlos (UFSCar), São Carlos, São Paulo 13565-905, Brazil;* orcid.org/0000-0001-6734-7381; Email: cgotoni@unicamp.br

Luiz Henrique Capparelli Mattoso – *Nanotechnology National Laboratory for Agriculture (LNNA), Embrapa Instrumentation, São Carlos, São Paulo 13561-206, Brazil;* orcid.org/0000-0001-7586-1014; Email: luiz.mattoso@embrapa.br

Authors

Amanda R. Sorigotti – *Nanotechnology National Laboratory for Agriculture (LNNA), Embrapa Instrumentation, São*

https://doi.org/10.1021/acsabm.6c00155
ACS Appl. Bio Mater. 2026, 9, 4170−4181

Carlos, São Paulo 13561-206, Brazil; orcid.org/0000-0002-9721-3111

Rafaella T. Paschoalin – *Nanotechnology National Laboratory for Agriculture (LNNA), Embrapa Instrumentation, São Carlos, São Paulo 13561-206, Brazil; São Carlos Institute of Physics (IFSC), University of São Paulo (USP), São Carlos, São Paulo 13566-590, Brazil*

Robson Rosa da Silva – *NanoScientifca Scandinavian AB, Gothenburg 41 390, Sweden*; orcid.org/0000-0001-6887-4749

Rafaella F. Fernandes – *Nanotechnology National Laboratory for Agriculture (LNNA), Embrapa Instrumentation, São Carlos, São Paulo 13561-206, Brazil*; orcid.org/0000-0002-0135-8528

Hernane da Silva Barud – *Centro Universitário de Araraquara (UNIARA), Araraquara, São Paulo 14801-320, Brazil*; orcid.org/0000-0001-9081-2413

Sidney J. L. Ribeiro – *Institute of Chemistry, São Paulo State University (UNESP), Araraquara, São Paulo 14800-900, Brazil*

Osvaldo N. Oliveira Jr – *São Carlos Institute of Physics (IFSC), University of São Paulo (USP), São Carlos, São Paulo 13566-590, Brazil*; orcid.org/0000-0002-5399-5860

Complete contact information is available at: https://pubs.acs.org/doi/10.1021/acsabm.6c00155

Funding

The Article Processing Charge for the publication of this research was funded by the Coordenacao de Aperfeicoamento de Pessoal de Nivel Superior (CAPES), Brazil (ROR identifier: 00x0ma614).

Notes

The authors declare no competing financial interest.

■ ACKNOWLEDGMENTS

This research was financed, in part, by the São Paulo Research Foundation (FAPESP, Brazil; 2017/22172-9, 2021/12071-6, 2025/27044-5), the National Council for Scientific and Technological Development (CNPq, Brazil) through the INCT Circularity in Polymer Materials (grant no. 406925/2022-4), INEO (408449/2024-1), and the Federal Agency for Support and Evaluation of Graduate Education (CAPES, Brazil; Finance Code 001). The authors are grateful for the facilities of the Brazilian National Nanotechnology Laboratory (LNNano)/Brazilian National Center for Research in Energy and Materials (CNPEM). C.G.O. acknowledges CNPq (grant no. 304753/2022-0). The National Institutes of Science and Technology (INCTs), IINCT-INFO (Photonics), and INCT NanoVida (Nanomaterials for Life) are also acknowledged.

■ REFERENCES

(1) Magaz, A.; Roberts, A. D.; Faraji, S.; Nascimento, T. R. L.; Medeiros, E. S.; Zhang, W.; Greenhalgh, R. D.; Mautner, A.; Li, X.; Blaker, J. J. Porous, Aligned, and Biomimetic Fibers of Regenerated Silk Fibroin Produced by Solution Blow Spinning. *Biomacromolecules* **2018**, *19* (12), 4542–4553.

(2) Paschoalin, R. T.; Traldi, B.; Aydin, G.; Oliveira, J. E.; Rütten, S.; Mattoso, L. H. C.; Zenke, M.; Sechi, A. Solution Blow Spinning Fibres: New Immunologically Inert Substrates for the Analysis of Cell Adhesion and Motility. *Acta Biomater.* **2017**, *51*, 161–174.

(3) da Silva Parize, D. D.; de Oliveira, J. E.; Foschini, M. M.; Marconcini, J. M.; Mattoso, L. H. C. Poly(Lactic Acid) Fibers Obtained by Solution Blow Spinning: Effect of a Greener Solvent on the Fiber Diameter *J. Appl. Polym. Sci.* **2016**, 133 (18).

(4) Abolhasani, S.; Ahmadi, Y.; Rostami, Y.; Baravar, E.; Fattahi, D. Biomaterials in Tissue Repair and Regeneration: Key Insights from Extracellular Matrix Biology. *Front. Med. Technol.* **2025**, *7*, No. 1565810.

(5) Chen, Z.; Du, C.; Liu, S.; Liu, J.; Yang, Y.; Dong, L.; Zhao, W.; Huang, W.; Lei, Y. Progress in Biomaterials Inspired by the Extracellular Matrix. *Giant* **2024**, *19*, No. 100323.

(6) Mangani, S.; Vetoulas, M.; Mineschou, K.; Spanopoulos, K.; Vivanco, M. dM.; Piperigkou, Z.; Karamanos, N. K. Design and Applications of Extracellular Matrix Scaffolds in Tissue Engineering and Regeneration. *Cells* **2025**, *14* (14), No. 1076.

(7) Pardo, A.; Gomez-Florit, M.; Davidson, M. D.; Öztürk-Öncel, M. Ö.; Domingues, R. M. A.; Burdick, J. A.; Gomes, M. E. Hierarchical Design of Tissue-Mimetic Fibrillar Hydrogel Scaffolds. *Adv. Healthc. Mater.* **2024**, *13* (16), No. 2303167.

(8) Cheng, F.; Song, D.; Li, H.; Ravi, S. K.; Tan, S. C. Recent Progress in Biomedical Scaffold Fabricated via Electrospinning: Design, Fabrication and Tissue Engineering Application. *Adv. Funct. Mater.* **2025**, *35* (1), No. 2406950.

(9) Haririan, Y.; Elahi, A.; Shadman-Manesh, V.; Rezaei, H.; Mohammadi, M.; Asefnejad, A. Advanced Nanostructured Biomaterials for Accelerated Wound Healing: Insights into Biological Interactions and Therapeutic Innovations: A Comprehensive Review. *Mater. Des.* **2025**, *258*, No. 114698.

(10) Song, J.; Liu, Z.; Li, Z.; Wu, H. Continuous Production and Properties of Mutil-Level Nanofiber Air Filters by Blow Spinning. *RSC. Adv.* **2020**, *10* (33), 19615–19620.

(11) Dias, F. T. G.; Rempel, S. P.; Agnol, L. D.; Bianchi, O. The Main Blow Spun Polymer Systems: Processing Conditions and Applications. *J. Polym. Res.* **2020**, *27* (8), 205.

(12) Rodrigues, M. Á. V.; Bertolo, M. R. V.; Horn, M. M.; Lugão, A. B.; Mattoso, L. H. C.; de Guzzi Plepis, A. M. Comparing Solution Blow Spinning and Electrospinning Methods to Produce Collagen and Gelatin Ultrathin Fibers: A Review. *Int. J. Biol. Macromol.* **2024**, *283*, No. 137806.

(13) Carriles, J.; Nguewa, P.; González-Gaitano, G. Advances in Biomedical Applications of Solution Blow Spinning. *Int. J. Mol. Sci.* **2023**, *24* (19), No. 14757.

(14) Jin, Y.; Hang, Y.; Luo, J.; Zhang, Y.; Shao, H.; Hu, X. In Vitro Studies on the Structure and Properties of Silk Fibroin Aqueous Solutions in Silkworm. *Int. J. Biol. Macromol.* **2013**, *62*, 162–166.

(15) Li, T.; Song, X.; Weng, C.; Wang, X.; Gu, L.; Gong, X.; Wei, Q.; Duan, X.; Yang, L.; Chen, C. Silk Fibroin/Carboxymethyl Chitosan Hydrogel with Tunable Biomechanical Properties Has Application Potential as Cartilage Scaffold. *Int. J. Biol. Macromol.* **2019**, *137*, 382–391.

(16) Laity, P. R.; Holland, C. Thermo-Rheological Behaviour of Native Silk Feedstocks. *Eur. Polym. J.* **2017**, *87*, 519–534.

(17) Laity, P. R.; Gilks, S. E.; Holland, C. Rheological Behaviour of Native Silk Feedstocks. *Polymer* **2015**, *67*, 28–39.

(18) Zhang, X.; Pan, Z. Rheological Behavior of Regenerated Silk Fibroin/Polyvinyl Alcohol Blended Solutions in Steady and Dynamic State and the Effect of Temperature. *J. Mater. Sci.* **2020**, *55* (31), 15350–15363.

(19) Zhu, J.; Zhang, Y.; Shao, H.; Hu, X. Electrospinning and Rheology of Regenerated *Bombyx* Mori Silk Fibroin Aqueous Solutions: The Effects of PH and Concentration. *Polymer* **2008**, *49* (12), 2880–2885.

(20) Zhao, M.; Qi, Z.; Tao, X.; Newkirk, C.; Hu, X.; Lu, S. Chemical, Thermal, Time, and Enzymatic Stability of Silk Materials with Silk I Structure. *Int. J. Mol. Sci.* **2021**, *22* (8), No. 4136.

(21) Rahman, M.; Dip, T. M.; Nur, M. G.; Padhye, R.; Houshyar, S. Fabrication of Silk Fibroin-Derived Fibrous Scaffold for Biomedical Frontiers. *Macromol. Mater. Eng.* **2024**, *309* (5), No. 2300422.

(22) Liu, B.; Li, Y.; Chen, H.; Li, S.; Dan, X.; Xue, P.; Li, Y.; Lei, L.; Fan, X. From Molecular Mechanisms to Clinical Translation: Silk Fibroin-Based Biomaterials for next-Generation Wound Healing. *Int. J. Biol. Macromol.* **2025**, *313*, No. 144266.
(23) Radulescu, D.-M.; Andronescu, E.; Vasile, O. R.; Ficai, A.; Vasile, B. S. Silk Fibroin-Based Scaffolds for Wound Healing Applications with Metal Oxide Nanoparticles. *J. Drug Delivery Sci. Technol.* **2024**, *96*, No. 105689.
(24) Wani, S. U. D.; Zargar, M. I.; Masoodi, M. H.; Alshehri, S.; Alam, P.; Ghoneim, M. M.; Alshlowi, A.; Shivakumar, H. G.; Ali, M.; Shakeel, F. Silk Fibroin as an Efficient Biomaterial for Drug Delivery, Gene Therapy, and Wound Healing. *Int. J. Mol. Sci.* **2022**, *23* (22), No. 14421.
(25) De Giorgio, G.; Matera, B.; Vurro, D.; Manfredi, E.; Galstyan, V.; Tarabella, G.; Ghezzi, B.; D'Angelo, P. Silk Fibroin Materials: Biomedical Applications and Perspectives. *Bioengineering* **2024**, *11* (2), No. 167.
(26) Kulhánková, J.; Hobbs, C. J.; Holubová, B. N.; Erben, J.; Rysová, M.; Musílková, J.; Svobodová, L.; Romanyuk, N.; Máková, V. Hybrid Fibres: A New Path in Tissue Regeneration. *J. Mater. Sci. Mater. Med.* **2025**, *36* (1), 29.
(27) Achalhi, N.; El Ouardi, Y.; El Yousfi, R.; Moumnassi, S.; El Barkany, S.; Asehraou, A.; El Idrissi, A. Single-Step Synthesis and Comprehensive Characterization of Hydroxyethyl Cellulose Grafted with (3-Aminopropyl)Triethoxysilane: Mechanistic Insights and Evaluation of Antimicrobial Properties. *Carbohydr. Polym.* **2025**, *360*, No. 123613.
(28) Zhong, J.; Liu, Y.; Ren, J.; Tang, Y.; Qi, Z.; Zhou, X.; Chen, X.; Shao, Z.; Chen, M.; Kaplan, D. L.; Ling, S. Understanding Secondary Structures of Silk Materials via Micro- and Nano-Infrared Spectroscopies. *ACS Biomater Sci. Eng.* **2019**, *5* (7), 3161–3183.
(29) Vladkova, T. G. Surface Engineered Polymeric Biomaterials with Improved Biocontact Properties. *Int. J. Polym. Sci.* **2010**, *2010*, 1–22.
(30) Rockwood, D. N.; Preda, R. C.; Yücel, T.; Wang, X.; Lovett, M. L.; Kaplan, D. L. Materials Fabrication from *Bombyx Mori* Silk Fibroin. *Nat. Protoc.* **2011**, *6* (10), 1612–1631.
(31) Ye, B.; Jia, C.; Li, Z.; Li, L.; Zhao, Q.; Wang, J.; Wu, H. Solution-blow Spun PLA/SiO_2 Nanofiber Membranes toward High Efficiency Oil/Water Separation. *J. Appl. Polym. Sci.* **2020**, *137* (37), No. 49103.
(32) Cui, X.; Wang, L.; Gao, X.; Wu, J.; Hu, T.; Zhang, J.; Zhou, X.; Zhang, K.-Q.; Cheng, L. Self-Assembled Silk Fibroin Injectable Hydrogels Based on Layered Double Hydroxides for Spinal Cord Injury Repair. *Matter* **2024**, *7* (2), 620–639.
(33) Oliveira, J. E.; Moraes, E. A.; Costa, R. G. F.; Afonso, A. S.; Mattoso, L. H. C.; Orts, W. J.; Medeiros, E. S. Nano and submicrometric fibers of poly(D,L-lactide) obtained by solution blow spinning: Process and solution variables. *J. Appl. Polym. Sci.* **2011**, *122* (5), 3396–3405.
(34) Wang, C.; Fang, H.; Hang, C.; Sun, Y.; Peng, Z.; Wei, W.; Wang, Y. Fabrication and Characterization of Silk Fibroin Coating on APTES Pretreated Mg-Zn-Ca Alloy. *Mater. Sci. Eng. C Mater. Biol. Appl.* **2020**, *110*, No. 110742.
(35) Saengdee, P.; Promptmas, C.; Thanapitak, S.; Srisuwan, A.; Pankiew, A.; Thornyanadacha, N.; Chaisriratanakul, W.; Chaowicharat, E.; Jeamsaksiri, W. Optimization of 3-Aminopropyltriethoxysilane Functionalization on Silicon Nitride Surface for Biomolecule Immobilization. *Talanta* **2020**, *207*, No. 120305.
(36) Sun, F.; Li, T.-T.; Zhang, X.; Shiu, B.-C.; Zhang, Y.; Ren, H.-T.; Peng, H.-K.; Lin, J.-H.; Lou, C.-W. In Situ Growth Polydopamine Decorated Polypropylen Melt-Blown Membrane for Highly Efficient Oil/Water Separation. *Chemosphere* **2020**, *254*, No. 126873.
(37) Kim, H.; Kwon, J.-Y. Enzyme Immobilization on Metal Oxide Semiconductors Exploiting Amine Functionalized Layer. *RSC Adv.* **2017**, *7* (32), 19656–19661.
(38) Chen, P.; Li, L.; Dong, L.; Wang, S.; Huang, Z.; Qian, Y.; Wang, C.; Liu, W.; Yang, L. Gradient Biomineralized Silk Fibroin Nanofibrous Scaffold with Osteochondral Inductivity for Integration of Tendon to Bone. *ACS Biomater Sci. Eng.* **2021**, *7* (3), 841–851.
(39) Sencadas, V. Influence of the Stabilization Process on the Piezotronic Performance of Electrospun Silk Fibroin. *Macromol. Mater. Eng.* **2020**, *305* (6), No. 2000165.
(40) Zhao, G.; Zhang, X.; Li, B.; Huang, G.; Xu, F.; Zhang, X. Solvent-Free Fabrication of Carbon Nanotube/Silk Fibroin Electrospun Matrices for Enhancing Cardiomyocyte Functionalities. *ACS Biomater. Sci. Eng.* **2020**, *6* (3), 1630–1640.
(41) Dehghan-Manshadi, N.; Fattahi, S.; Hadizadeh, M.; Nikukar, H.; Moshtaghioun, S. M.; Aflatoonian, B. The Influence of Elastomeric Polyurethane Type and Ratio on the Physicochemical Properties of Electrospun Polyurethane/Silk Fibroin Hybrid Nanofibers as Potential Scaffolds for Soft and Hard Tissue Engineering. *Eur. Polym. J.* **2019**, *121*, No. 109294.
(42) Pavlova, E. R.; Bagrov, D. V.; Monakhova, K. Z.; Piryazev, A. A.; Sokolova, A. I.; Ivanov, D. A.; Klinov, D. V. Tuning the Properties of Electrospun Polylactide Mats by Ethanol Treatment. *Mater. Des.* **2019**, *181*, No. 108061.
(43) Hofmann, E.; Dulle, M.; Liao, X.; Greiner, A.; Förster, S. Controlling Polymer Microfiber Structure by Micro Solution Blow Spinning. *Macromol. Chem. Phys.* **2020**, *221* (1), No. 1900453.
(44) Richard-Lacroix, M.; Pellerin, C. Molecular Orientation in Electrospun Fibers: From Mats to Single Fibers. *Macromolecules* **2013**, *46* (24), 9473–9493.
(45) da Silva Parize, D. D.; Foschini, M. M.; de Oliveira, J. E.; Klamczynski, A. P.; Glenn, G. M.; Marconcini, J. M.; Mattoso, L. H. C. Solution Blow Spinning: Parameters Optimization and Effects on the Properties of Nanofibers from Poly(Lactic Acid)/Dimethyl Carbonate Solutions. *J. Mater. Sci.* **2016**, *51* (9), 4627–4638.
(46) Liu, W.; Lipner, J.; Moran, C. H.; Feng, L.; Li, X.; Thomopoulos, S.; Xia, Y. Generation of Electrospun Nanofibers with Controllable Degrees of Crimping Through a Simple, Plasticizer-Based Treatment. *Adv. Mater.* **2015**, *27* (16), 2583–2588.
(47) Holland, C.; Terry, A. E.; Porter, D.; Vollrath, F. Comparing the Rheology of Native Spider and Silkworm Spinning Dope. *Nat. Mater.* **2006**, *5* (11), 870–874.
(48) Boulet-Audet, M.; Terry, A. E.; Vollrath, F.; Holland, C. Silk Protein Aggregation Kinetics Revealed by Rheo-IR. *Acta Biomater.* **2014**, *10* (2), 776–784.
(49) Rošic, R.; Pelipenko, J.; Kocbek, P.; Baumgartner, S.; Bešter-Rogač, M.; Kristl, J. The Role of Rheology of Polymer Solutions in Predicting Nanofiber Formation by Electrospinning. *Eur. Polym. J.* **2012**, *48* (8), 1374–1384.
(50) Gong, L.; Chase, D. B.; Noda, I.; Liu, J.; Martin, D. C.; Ni, C.; Rabolt, J. F. Discovery of β-Form Crystal Structure in Electrospun Poly[(R)-3-Hydroxybutyrate-Co-(R)-3-Hydroxyhexanoate] (PHBHx) Nanofibers: From Fiber Mats to Single Fibers. *Macromolecules* **2015**, *48* (17), 6197–6205.
(51) Dazzi, A.; Prater, C. B. AFM-IR: Technology and Applications in Nanoscale Infrared Spectroscopy and Chemical Imaging. *Chem. Rev.* **2017**, *117* (7), 5146–5173.
(52) Xiao, L.; Schultz, Z. D. Spectroscopic Imaging at the Nanoscale: Technologies and Recent Applications. *Anal. Chem.* **2018**, *90* (1), 440–458.
(53) Barth, A. Infrared Spectroscopy of Proteins. *Biochim. Biophys. Acta, Bioenerg.* **2007**, *1767* (9), 1073–1101.
(54) Ling, S.; Qi, Z.; Knight, D. P.; Shao, Z.; Chen, X. Synchrotron FTIR Microspectroscopy of Single Natural Silk Fibers. *Biomacromolecules* **2011**, *12* (9), 3344–3349.
(55) Kaur, A.; Kapoor, S.; Bharti, A.; Rana, S.; Chaudhary, G. R.; Prabhakar, N. Gold-platinum Bimetallic Nanoparticles Coated 3-(Aminopropyl)Triethoxysilane (APTES) Based Electrochemical Immunosensor for Vitamin D Estimation. *J. Electroanal. Chem.* **2020**, *873*, No. 114400.
(56) Shao, J.; Zheng, J.; Liu, J.; Carr, C. M. Fourier Transform Raman and Fourier Transform Infrared Spectroscopy Studies of Silk Fibroin. *J. Appl. Polym. Sci.* **2005**, *96* (6), 1999–2004.
(57) da Silva, R. R.; Cavicchioli, M.; Lima, L. R.; Otoni, C. G.; Barud, H. S.; Santagneli, S. H.; Tercjak, A.; Amaral, A. C.; Carvalho, R. A.; Ribeiro, S. J. L. Fabrication of Biocompatible, Functional, and Transparent Hybrid Films Based on Silk Fibroin and Epoxy Silane for Biophotonics. *ACS Appl. Mater. Interfaces* **2017**, *9* (33), 27905–27917.

https://doi.org/10.1021/acsabm.6c00155
ACS Appl. Bio Mater. 2026, 9, 4170–4181

(58) Sagnella, A.; Zambianchi, M.; Durso, M.; Posati, T.; Del Rio, A.; Donnadio, A.; Mazzanti, A.; Pistone, A.; Ruani, G.; Zamboni, R.; Benfenati, V.; Melucci, M. APTES Mediated Modular Modification of Regenerated Silk Fibroin in a Water Solution. *RSC Adv.* **2015**, *5* (78), 63401–63406.
(59) DeFlores, L. P.; Ganim, Z.; Nicodemus, R. A.; Tokmakoff, A. Amide I′–II′ 2D IR Spectroscopy Provides Enhanced Protein Secondary Structural Sensitivity. *J. Am. Chem. Soc.* **2009**, *131* (9), 3385–3391.
(60) Yang, H.; Lai, C.; Xuan, C.; Chai, M.; Liu, X.; Chen, Y.; Shi, X. Integrin-Binding pro-Survival Peptide Engineered Silk Fibroin Nanosheets for Diabetic Wound Healing and Skin Regeneration. *Chem. Eng. J.* **2020**, *398*, No. 125617.
(61) Qi, Y.; Wang, H.; Wei, K.; Yang, Y.; Zheng, R.-Y.; Kim, I.; Zhang, K.-Q. A Review of Structure Construction of Silk Fibroin Biomaterials from Single Structures to Multi-Level Structures. *Int. J. Mol. Sci.* **2017**, *18* (3), No. 237.
(62) Um, I. C.; Kweon, H. Y.; Lee, K. G.; Park, Y. H. The Role of Formic Acid in Solution Stability and Crystallization of Silk Protein Polymer. *Int. J. Biol. Macromol.* **2003**, *33* (4−5), 203–213.
(63) Liu, J.; Chen, H.; Wang, Y.; Li, G.; Zheng, Z.; Kaplan, D. L.; Wang, X.; Wang, X. Flexible Water-Absorbing Silk-Fibroin Biomaterial Sponges with Unique Pore Structure for Tissue Engineering. *ACS Biomater Sci. Eng.* **2020**, *6* (3), 1641–1649.
(64) Lu, Q.; Hu, X.; Wang, X.; Kluge, J. A.; Lu, S.; Cebe, P.; Kaplan, D. L. Water-Insoluble Silk Films with Silk I Structure. *Acta Biomater.* **2010**, *6* (4), 1380–1387.
(65) Hu, Z.; Das, S. K.; Yan, S.; You, R.; Li, X.; Luo, Z.; Li, M.; Zhang, Q.; Kaplan, D. L. Stability and Biodegradation of Silk Fibroin/Hyaluronic Acid Nerve Conduits. *Composites, Part B* **2020**, *200*, No. 108222.
(66) Jiang, Q.; Xu, Y.; Chen, M.; Meng, Q.; Zhang, C. Modification of the wood-plastic composite for enhancement of formaldehyde clearance and the 3D printing application. *J. Appl. Polym. Sci.* **2021**, *138* (3), No. 49683.

https://doi.org/10.1021/acsabm.6c00155
ACS Appl. Bio Mater. 2026, 9, 4170−4181